Materials Advances

PAPER

Cite this: *Mater. Adv.*, 2022, **3**, 232

CeO_2/CuO/3DOM SiO_2 catalysts with very high efficiency and stability for CO oxidation†

Chao Miao,[ab] Lingling Zhang,[ab] Weimin Xie,[ab] Lixing Liang,[ab] Shumei Chen,[ab] Yi Zhang *[ab] and Jing Ouyang *[abc]

Received 7th September 2021,
Accepted 7th October 2021

DOI: 10.1039/d1ma00817j

rsc.li/materials-advances

Based on the urgent need for highly active and stable catalysts for CO conversion at low temperature, a CeO_2/CuO/SiO_2 ordered macroporous composite catalyst with a 3DOM structure was prepared. The 3DOM matrix possesses a fairly high specific surface area of 598 m^2 g^{-1} and a large pore size of 250-300 nm, which stably assembles CeO_2 and CuO nanoparticles but without clogging the pores. The 0.5CeO_2/0.25CuO/3DOM SiO_2 catalyst exhibits excellent catalytic activity to CO, due to the synergistic effect of CeO_2, CuO and metal–support interactions. The conversion of CO can reach 100% at 160 °C and maintain excellent stability up to 12 h, due to the abundant lattice oxygen vacancies in CeO_2. The adsorption behavior of CO molecules on the 0.5CeO_2/0.25CuO/3DOM catalyst was further confirmed by *in situ* Fourier transform infrared spectroscopy, and the possible mechanism of CO oxidation was explained.

1. Introduction

Nowadays, air pollution caused by CO, such as in the cases of environmental emergency in core mining, metallurgy exhausts, and diesel submarine atmosphere, is extremely harmful to the environment and human health.[1,2] The influences of CO pollution, that is one of the most poisonous pollutions, need to be reduced or even eliminated imminently. The oxidation reaction of CO is a key step and also an effective method to reduce its negative effects.[3,4]

The CO catalytic oxidation has a series of advantages such as low energy consumption, high processing capacity and low secondary pollution, which show its superiority to many CO removal technologies.[5–7] Moreover, CO catalytic oxidation can be used as a typical model reaction to study the gas-solid interface reaction in multiphase catalysis.[8–10] The traditional noble metal–based CO oxidation catalysts show excellent CO oxidation activity, but it is difficult to realize large-scale application due to the scarcity and high price of noble metals.[8,9,11] In recent years, catalysts composed of transition metals and rare earth metal-oxide composite materials have been widely studied in CO catalytic oxidation.[2–4,12] Extensive research has demonstrated that reducible metal oxides such as CeO_2/CuO and their composite catalysts possess high CO oxidation properties, which can make them appropriate candidates for high-activity noble metal oxidation catalysts, and due to their low price, they are expected to replace the noble metal-based catalyst.[13,14]

The uniqueness of applying CeO_2 in catalysts lies in the high concentration of oxygen vacancies, which endow high oxygen storage and release capabilities, and effectively provide oxygen to the catalytic reaction.[8,15,16] In addition, there are two main valence states of Ce including Ce^{3+} and Ce^{4+} in cerium oxide. The interaction between Ce^{3+} and Ce^{4+} can provide very high catalytic activity for surface redox reactions.[14,17] However, due to the weak oxidation mobility and easy sintering of pure CeO_2, it is often doped or mixed with other metals to improve the catalytic performance. The transition metal Cu is also an element with good valence changing properties (Cu^+/Cu^{2+}), but its catalytic activity for CO oxidation is low when used as a single catalyst and needs to be further composited with other metals to improve its performance.[18,19] Recently, CeO_2–CuO mixed oxides have received great attention due to their high activity, selectivity and persistence for CO catalytic oxidation. The substantial literature has proved that the interaction between CeO_2 and CuO could improve the catalytic oxidation performance toward CO.[20–22] Since the radius of the Ce atom is larger than that of the Cu, the latter can be doped into the lattice of CeO_2.[23] The doping and modification of CuO can form

---

[a] Hunan Key Lab of Mineral Materials and Application, Central South University, Changsha 410083, China. E-mail: yee_z10@csu.edu.cn, jingouyang@csu.edu.cn; Fax: +86-731-8871-0804; Tel: +86-731-8883-0549

[b] Centre for Mineral Materials, Department of Inorganic Materials, School of Minerals Processing and Bioengineering, Central South University, Changsha 410083, China

[c] Key Lab of Clay Mineral Functional Materials in China Building Materials Industry, Central South University, Changsha 410083, China

† Electronic supplementary information (ESI) available: The detailed characterizations and Catalytic activity testing parameters as well as the FTIR acquisition spectra of series samples. See DOI: 10.1039/d1ma00817j

Cu^{x+}–Ce^{3+}–Ce^{4+} configuration and simultaneously create an unsaturated second-phase CuO, which will increase the defect concentration in the material (such as oxygen vacancies), generate extra electrons, and make the gaseous oxygen molecule around the material to be adsorbed and converted into active oxygen atoms to improve the efficiency of CO catalytic oxidation.[19,24,25] In addition, the catalyst support will affect the catalytic performance. The three-dimensional ordered macroporous material (3DOM), with an open, uniform and interconnected three-dimensional void structure, efficient mass transfer efficiency and high surface accessibility, is a promising support in heterogeneous catalytic reactions.[26–28] Assembling other functional components inside the 3DOM support and designing functional 3DOM materials with special applications can ensure that the guest molecules can easily enter the internal pores of the material and release the active sites, hence the resistance to molecular diffusion will be greatly decreased.

Herein, we report the preparation of 3DOM SiO_2 by a colloidal crystal template method using PS microspheres as templates and tetraethyl orthosilicate (TEOS) as an organic silicon source. The CeO_2/CuO was loaded by a simple grinding calcination method for efficient catalytic oxidation of CO. We studied the phase structure, microstructure and surface chemical state of the composite catalysts and focused on the effect of different proportions of Ce and Cu loading on the physicochemical properties and catalytic activity of CeO_2/CuO/3DOM SiO_2 nanocomposites, aiming to design an effective and stable non-noble metal catalyst for low-temperature CO oxidation catalyst.

2. Experimental

Material preparation and methods

Polystyrene (PS) microspheres were prepared by soap-free emulsion polymerization. First, the monodisperse PS microspheres were synthesized by surfactant-free emulsion polymerization, and then the colloidal crystal template was formed by a centrifugal assembly strategy similar to the method of Tian *et al.*[29] The 3DOM SiO_2 material used TEOS as the precursor. In a typical synthesis procedure, 6.24 g TEOS, 5.40 g ethanol, 0.97 g H_2O, and 0.89 g 37 wt% HCl were mixed and stirred for 15 min. Then, 0.8 g pre-prepared PS microsphere template was added and allowed to stand at room temperature for 24 h. The obtained sol-state liquid was subjected to procedures such as suction filtration, water washing, drying, and calcination to obtain 3DOM SiO_2 materials. In addition, the calcination procedure involves 350 °C calcination for 2 h, heating to 600 °C and then calcination for 2 h at a heating rate of 5 °C min^{-1}. The CeO_2/CuO/3DOM SiO_2 composite catalyst was prepared by a simple grinding and calcination method. First, a certain amount of $Ce(NO_3)_3{\cdot}6H_2O$ and $Cu(NO_3)_2{\cdot}3H_2O$ were weighed in proportion and ground into powder, then 3DOM SiO_2 was added, grounded and mixed well. The obtained mixture was calcined at 450 °C for 4 h at a heating rate of 5 °C min^{-1}. The ratio of the two nitrates was adjusted to obtain CeO_2/CuO/3DOM SiO_2 composites with different loading contents. The preparation procedure is schematically shown in Fig. 1, and the content and proportion of cerium and copper of CeO_2/CuO/3DOM SiO_2 series catalysts are given in Table 1.

Table 1 Content and mass proportion of cerium oxide and copper oxide in CeO_2/CuO/3DOM SiO_2 series catalysts

Samples	CeO_2/g	CuO/g	CeO_2/ CuO	CeO_2/CuO/ SiO_2
1CeO_2/0.5CuO/3DOM SiO_2	0.1	0.05	2 : 1	1 : 0.5 : 1
0.5CeO_2/0.5CuO/3DOM SiO_2	0.05	0.05	1 : 1	0.5 : 0.5 : 1
0.5CeO_2/0.25CuO/3DOM SiO_2	0.05	0.025	2 : 1	0.5 : 0.25 : 1
0.25CeO_2/0.25CuO/3DOM SiO_2	0.025	0.025	1 : 1	0.25 : 0.25 : 1
1CeO_2/3DOM SiO_2	0.1	0	1 : 0	1 : 0 : 1
1CuO/3DOM SiO_2	0	0.1	0 : 1	0 : 1 : 1
0.25CeO_2/0.5CuO/3DOM SiO_2	0.025	0.05	1 : 2	0.25 : 0. 5 : 1
0.75CeO_2/0.25CuO/3DOM SiO_2	0.075	0.025	3 : 1	0.75 : 0.25 : 1

3. Results and discussions

3.1 Characterizations of catalysts

In order to determine the conditions of the preparation process of the catalysts, the thermal behaviors of PS microspheres and nitrate/3DOM SiO_2 samples were analyzed under air atmosphere (Fig. 2). The PS microspheres begin to lose weight at about 250 °C and almost keep constant after 600 °C (Fig. 2a). The total weight loss rate of PS microspheres is about 93%, which mainly includes two processes. The weight loss in the first stage (250–400 °C) is about 83.1%, and two significant endothermic peaks are observed in this range. The first endothermic peak could be attributed to the fracture of the polymer, and the second endothermic peak is mainly caused by the carbonization, decomposition and volatilization of polystyrene.[30,31] The weight loss of the second stage (400–600 °C)

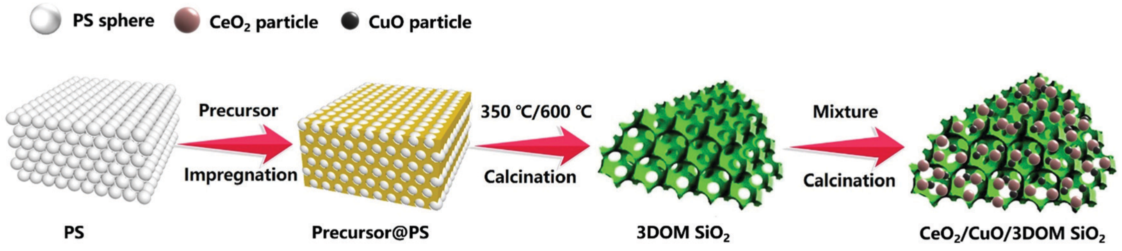

Fig. 1 Schematic of the preparation procedure of CeO_2/CuO/3DOM SiO_2.

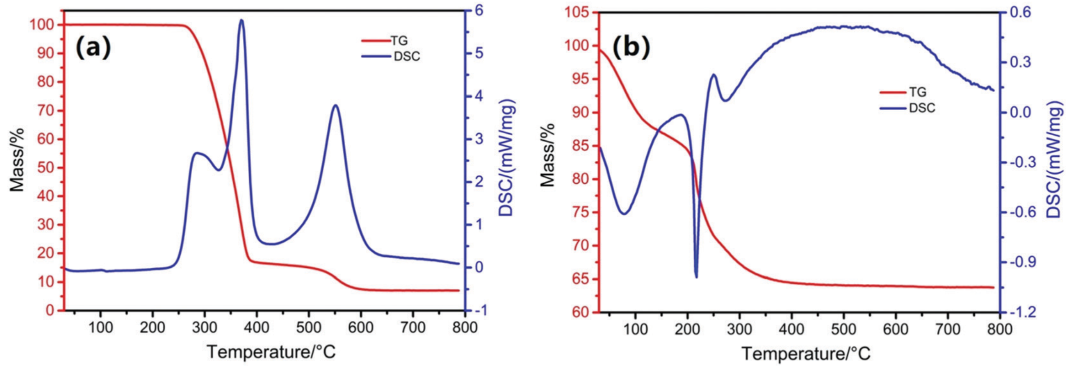

Fig. 2 TG-DSC curves of (a) PS microspheres and (b) nitrate/3DOM SiO_2 catalysts under air flow.

is about 8.9%, which is caused by the low degree graphitization of carbon combustion generated by polystyrene during the carbonization process.[32] The thermo-gravimetric analysis of the PS microspheres shows that the PS microsphere template can be completely burned at about 600 °C in air atmosphere. It is reasonable to determine that the removal temperature is 350 °C and 600 °C. The polymer can be fully broken and volatilized at 350 °C and then calcined at 600 °C to ensure the complete removal of the remaining hard-to-decompose substances. The weight loss of nitrate/3DOM SiO_2 in the temperature range is 36% (Fig. 2b), which could be attributed to the thermal decomposition of cerium and copper nitrates to produce metal oxides. The weight loss occurring at about 30–227 °C is mainly due to the evaporation and decomposition of hydroxyls in the raw sources when being heated. The weight loss rate at this stage is about 20%. The second stage of weight loss in the range 220–450 °C is accompanied with a weight loss of about 16%, which is mainly ascribed to the decomposition of nitrates into oxides. It indicates that 450 °C is the appropriate calcination temperature for the preparation of the catalysts.

The XRD spectra of 3DOM SiO_2 and those loaded with different contents of cerium and copper are shown in Fig. 3. There is no presence of crystal structural characteristic peaks in 3DOM SiO_2 (Fig. 3a), except for a wide peak packet observed at $2\theta = 22^\circ$, belonging to the amorphous SiO_2 structure. In addition, the XRD patterns of other four 3DOM SiO_2 with different CeO_2 loadings (Fig. 3a) indicate that CeO_2 in the four samples is a cubic fluorite structure (PDF JCPDS#34-0394).[24] The diffraction peaks of 1CuO/3DOM SiO_2 shown in Fig. 3b could be designated as the monoclinic CuO structure (PDF JCPDS#48-1548).[33,34] Comparing the positions of the (110) characteristic peaks of CeO_2 in the XRD patterns of different samples, a slight shift of about 0.16° can be detected on the three mixed oxide samples (inset in Fig. 3a). A similar phenomenon also appears in Fig. 3b, where the CuO $(11\bar{1})$ diffraction peaks of the three mixed oxide samples shifted to a certain extent (0.058°), compared to 1CuO/3DOM SiO_2 (inset in Fig. 3b). This may be originated from the smaller radius of Cu^{2+} than that of Ce^{4+} (0.073 nm for the former and 0.101 nm for the latter), which leads to the Cu^{2+} partial doping into the lattice of CeO_2 and causes the lattice expansion of CeO_2.[35,36] In addition, the relative intensities of XRD peaks of CeO_2 and CuO in all samples are proportional to their loading contents, which is consistent with the actual situation.

Fig. 4 shows the N_2 adsorption–desorption isotherm and pore size distribution of 3DOM SiO_2 and CeO_2/CuO/3DOM SiO_2 series catalysts, and the relevant pore structure data are attached in Table 2. The specific surface area of 3DOM SiO_2 is 598 $m^2\ g^{-1}$ and the pore volume is 0.591 $cm^3\ g^{-1}$. The larger specific surface area and pore volume will provide various

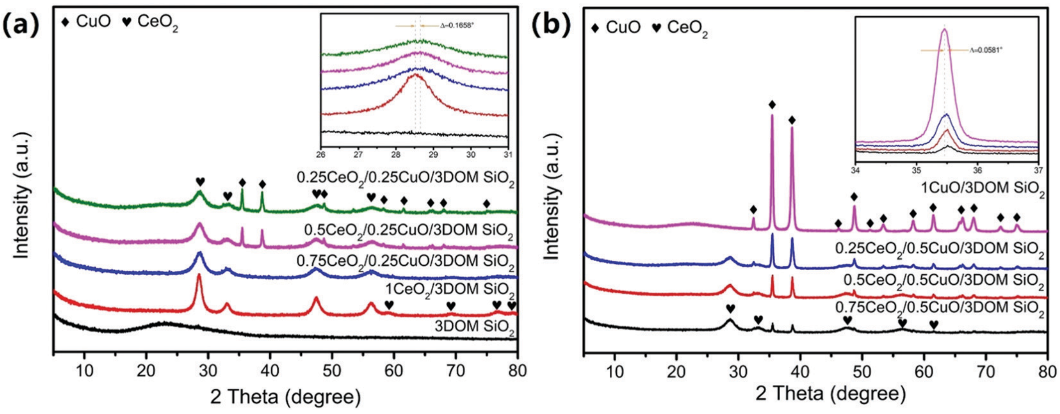

Fig. 3 XRD patterns of CeO_2/CuO/3DOM SiO_2 series catalysts: (a) loaded with different contents of CeO_2 (inset: amplified patterns in 26–31°) and (b) loaded with different contents of CuO (inset: amplified patterns in 34–37°).

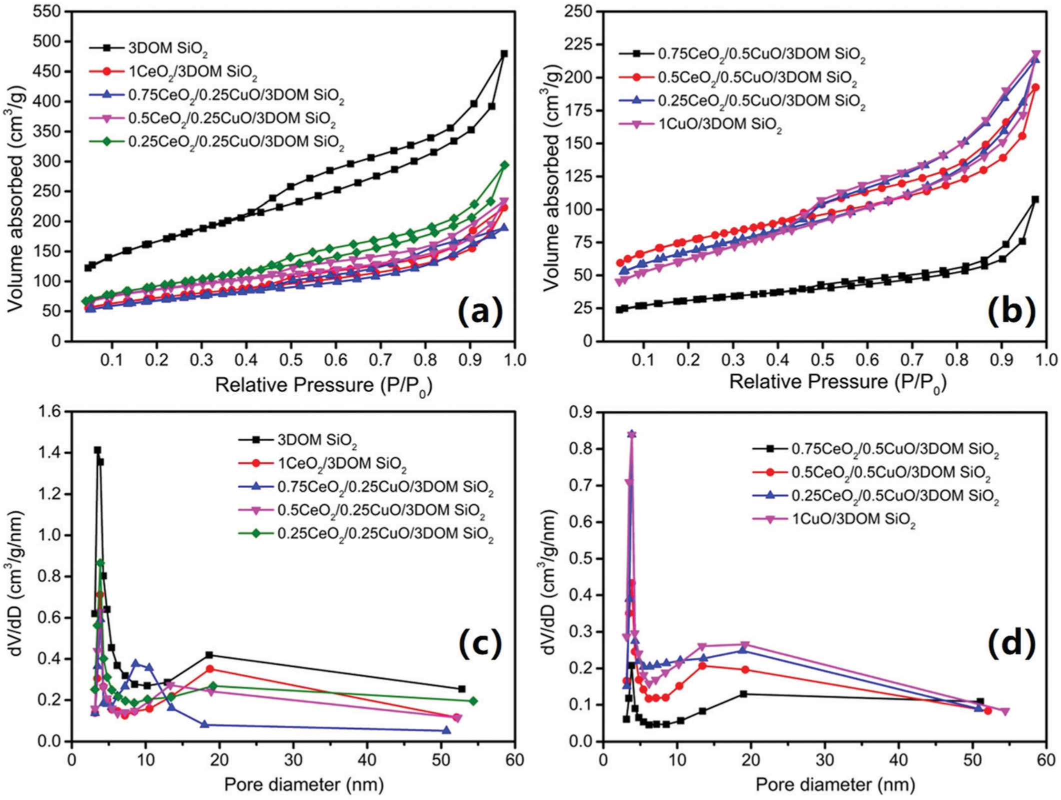

Fig. 4 N_2 adsorption–desorption isotherms (a and b), and pore size distribution of $CeO_2/CuO/3DOM\ SiO_2$ series catalysts (c and d).

Table 2 Specific surface area, pore size and pore volume of $CeO_2/CuO/3DOM\ SiO_2$ series catalysts

Samples	Surface area ($m^2\ g^{-1}$)	Average pore diameter (nm)	V_{tot} ($cm^3\ g^{-1}$)
3DOM SiO_2	598	3.5	0.59
$CeO_2/0.5CuO/3DOM\ SiO_2$	111	3.8	0.13
$0.5CeO_2/0.5CuO/3DOM\ SiO_2$	273	3.8	0.22
$0.5CeO_2/0.25CuO/3DOM\ SiO_2$	312	3.9	0.27
$0.25CeO_2/0.25CuO/3DOM\ SiO_2$	330	3.8	0.37
$0.1CeO_2/3DOM\ SiO_2$	260	3.8	0.28
$0.1CuO/3DOM\ SiO_2$	225	3.8	0.30
$0.25CeO_2/0.5CuO/3DOM\ SiO_2$	245	3.8	0.27
$0.75CeO_2/0.25CuO/3DOM\ SiO_2$	244	3.9	0.23

active sites for the catalytic reaction and can serve as an excellent support for nanoparticles.[3] Obviously, the $CeO_2/CuO/3DOM\ SiO_2$ catalysts show significant hysteresis loops in the relative pressure range of 0.5–1.0, but there is no type IV isotherm platform at high P/P_0, indicating that the samples contain a certain amount of mesopores (responsible for the hysteresis loops) and numerous macropores (resulting in the lack of platform for type IV isotherms).[2,37] The existence of H3-type hysteresis rings indicates that a certain number of small voids exist in 3DOM SiO_2, which should be the mesopores produced by the tangential parts among PS microspheres. Hence, the loop is consistent with the morphology of the prepared porous materials. At $P/P_0 = 0.45$, the desorption is forced to lock-in due to the "tensile strength effect". This indicates that the $CeO_2/CuO/3DOM\ SiO_2$ series of catalysts have a certain number of apparent mesopores (∼5 nm).[38] The volume absorbance near $P/P_0 = 1.0$ indicates that the total porosity of the catalyst has reached the macropore size range (about 300 nm), which is in line with the reality.[39,40] For 3DOM SiO_2 loaded with different contents of Ce and Cu (Fig. 4a and b), the spore volume decreased with the increase in the loading amount, which may be caused by the accumulation of CeO_2 and CuO nanoparticles on the pore wall of original 3DOM SiO_2. As a result, the macroporous–mesoporous structure of $CeO_2/CuO/3DOM\ SiO_2$ series catalysts was determined. According to the desorption branch of the isotherms, the corresponding pore size distribution curves were measured by the BJH method, which displays a sharp narrow peak of about 5 nm and a gentle broad peak in the range of 10–50 nm. It indicates that the catalysts have pores of about 4–6 nm diameter, while the gentle broad peak demonstrates that the catalysts have numerous larger pores with a relatively wide pore size distribution. Combined with the results of the SEM picture in Fig. 5e, 3DOM SiO_2 has a uniform (about 200 nm) pore size. The SEM images also show that there are still a large number of smaller channels inside the three-dimensional pore structure, which corresponds to the pore size distribution results.

3.2 Surface morphology analysis

The SEM images of the PS microsphere template confirm that the PS microspheres prepared in this experiment are highly orderly arranged (Fig. 5a). In addition, the prepared PS

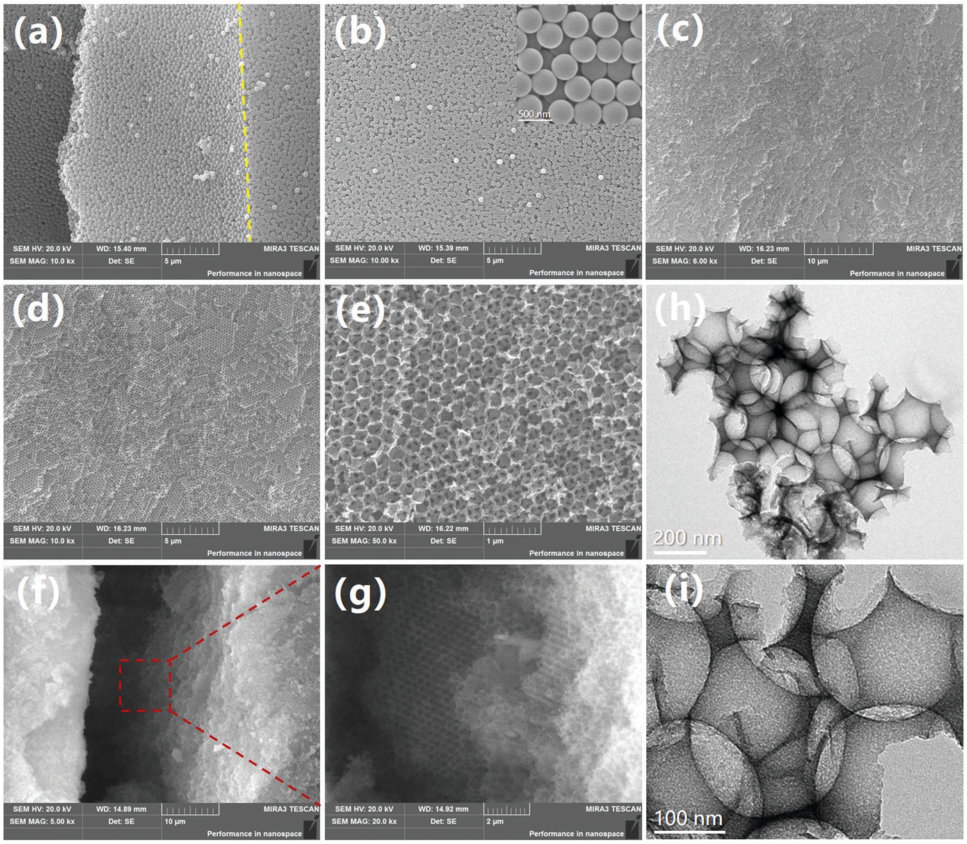

Fig. 5 (a and b) SEM images of PS microspheres and (c–g) 3DOM SiO_2 catalyst. (h and i) TEM images of 3DOM SiO_2 catalyst.

microspheres are complete and full spheres with a relatively uniform particle size, the diameter being about 350–400 nm (Fig. 5b, inset is the enlarged view). The SEM image of 3DOM SiO_2 shows that the catalyst has a three-dimensional ordered macroporous structure (Fig. 5c–e), and the overall structure is highly ordered face-centered cubic (FCC). The inner structure of macroporous 3DOM SiO_2 is opposite to the structure of the PS microsphere template and shows an inverted opal structure. In addition, the thickness of the pore wall is moderate, and the pore channels are neatly arranged, regular, and interconnected. Combined with the pore size distribution in Fig. 4c and d, the pore size of the openings on the 3DOM SiO_2 surface is uniform, with an average size of about 250–300 nm, which is in consistent with the SEM results. Compared with the PS

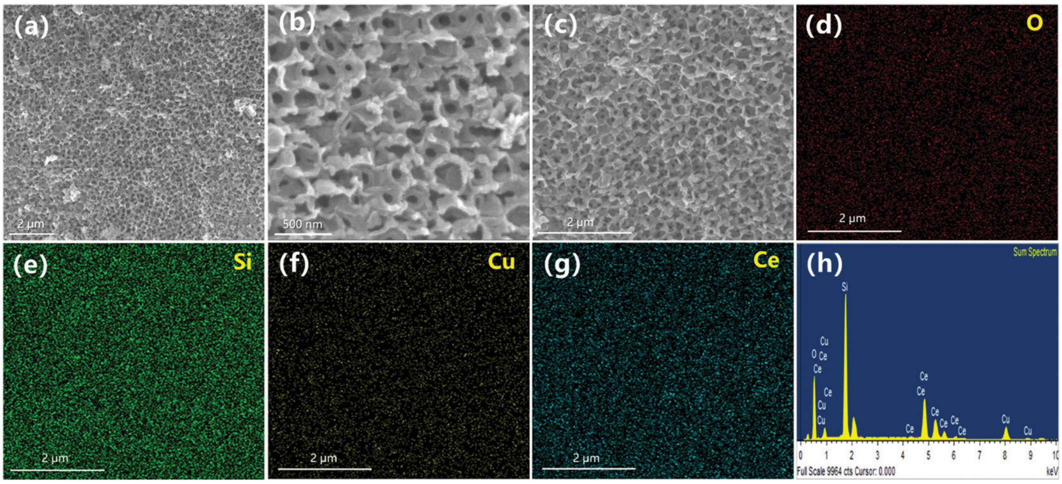

Fig. 6 (a–c) SEM images of $0.5CeO_2/0.25CuO/3DOM\ SiO_2$ catalyst and elemental mappings of (d) O, (e) Si, (f) Cu, (g) Ce and (h) EDS spectrum of the regions in (c).

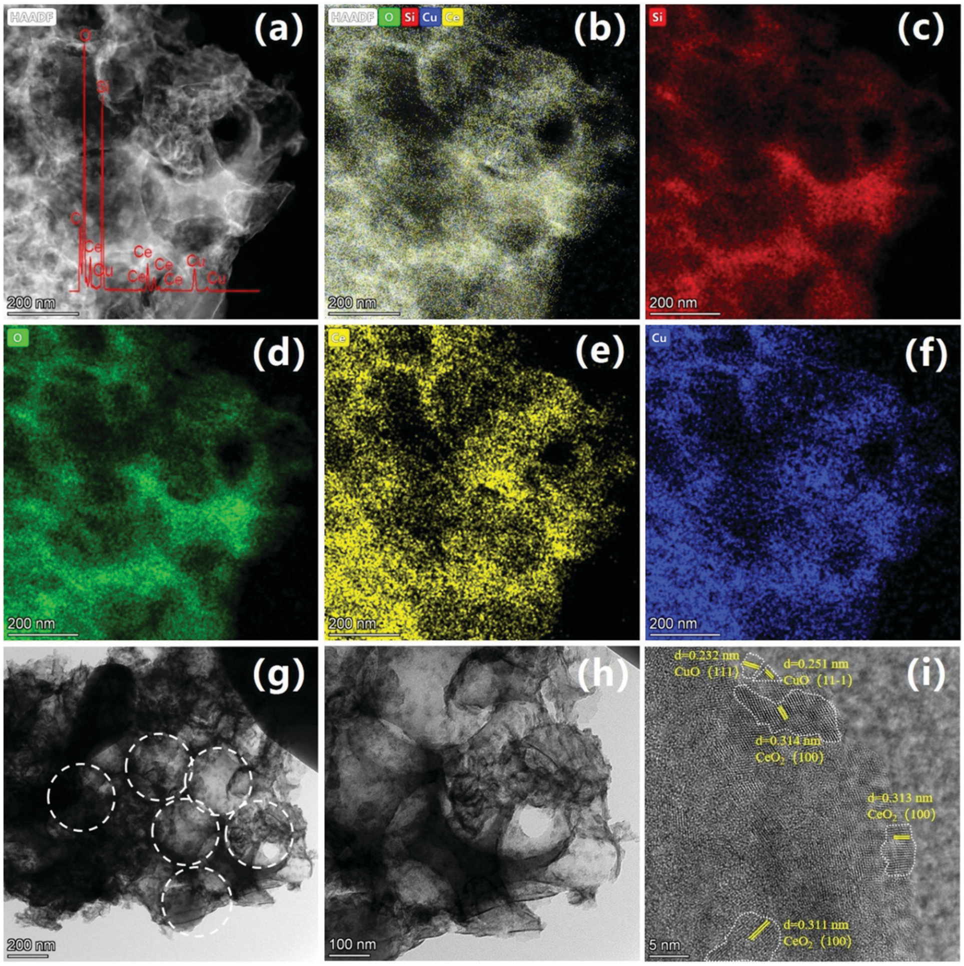

Fig. 7 (a) HAADF-STEM image of $0.5CeO_2/0.25CuO/3DOM\ SiO_2$ (the inset is the EDS spectrum). (b–f) Elemental mappings of $0.5CeO_2/0.25CuO/3DOM\ SiO_2$. (g and h) TEM images at different magnifications. (i) HRTEM image of random area in (h).

microsphere template, the pore size decreased by about 25%, which is mainly caused by the shrinkage of the Si skeleton during the high-temperature calcination.

Fig. 5f shows the SEM image of the cross section of 3DOM SiO_2, and Fig. 5g displays the enlarged image. Obviously, the internal structure of 3DOM SiO_2 is also highly ordered, and the pore and window among the macropores are interconnected. To observe the microstructure of 3DOM SiO_2 in more detail, a transmission electron microscope (TEM) was used to characterize the catalyst (Fig. 5h and i). It can be seen that the catalyst presented an ordered macroporous structure with a three-dimensional connected macroporous network, consistent with the results observed by SEM.

The morphology, structure and element distribution of the $0.5CeO_2/0.25CuO/3DOM\ SiO_2$ catalyst were observed by SEM, HAADF elemental mapping and EDS energy spectrum (Fig. 6a and b). It can be observed that the catalyst loaded with CeO_2 and CuO still maintains a 3DOM structure similar to that of 3DOM SiO_2, and the channel distribution is still uniform. Furthermore, it is also found that the pore wall thickness of the 3DOM material was significantly increased compared to the unloaded matrix. This is originated from the uniform loading of cerium copper oxide on the pore walls. The element distribution diagram of the catalyst revealed that Ce and Cu elements are evenly dispersed on the surface of the catalyst (Fig. 6d–g), indicating that the distribution of CeO_2 and CuO nanoparticles is relatively uniform on the framework of the 3DOM structure. Moreover, the peaks of Si, O, Ce and Cu can be observed in the EDS spectrum (Fig. 6h), which also demonstrates that the CeO_2 and CuO nanoparticles are successful loaded on the 3DOM SiO_2 matrix.

The microstructural features of the $0.5CeO_2/0.25CuO/3DOM\ SiO_2$ catalyst were further investigated by STEM and HRTEM. The HAADF-STEM image (Fig. 7a, illustrated for the EDS spectrum) and the EDX element mapping results (Fig. 7b–f) proved the existence of Si, Ce and Cu, and the uniform distribution without agglomeration can be concluded, which indicates the efficient assembly of CeO_2 and CuO in the 3DOM SiO_2 catalyst. Meanwhile, the distribution of Ce and Cu elements around the SiO_2 structure also presents a three-dimensionally ordered distribution, indicating that the load of CeO_2 and CuO did not change the microstructure of the matrix itself. Fig. 7g and h shows the typical TEM images of the $0.5CeO_2/0.25CuO/3DOM\ SiO_2$ catalyst at different magnifications. Distinct macropores with a diameter of 250–300 nm were observed, and some CeO_2 and CuO nanoparticles can be observed in the macropore. The HRTEM image was used to characterize the hybrid structure of the metal oxide on the catalyst surface (Fig. 7i). The lattice stripes in the region marked by the dotted line show the different crystal surfaces of CeO_2 and CuO. The *d* spacing values of the lattice stripes in the dotted line region (belongs to the (100) plane) are estimated to be 0.313 nm, which are attributed to fluorite CeO_2 (JCPDS PDF#34-0394),[24] while the estimated values of the *d* lattice spacing stripes are 0.232 nm and 0.251 nm, which belongs to the CuO(111) and $(11\bar{1})$ facets of black copper ore structure CuO (JCPDS PDF#48-1548).[33,34] Due to the polycrystalline nature of the sample, the lattice stripes of the two metal oxides on the surface of the catalyst are also randomly distributed on different crystal facets, and the amorphous structure below them is the SiO_2 matrix.

3.3 Surface XPS analysis

The surface composition and chemical bonds of the $0.5CeO_2/0.25CuO/3DOM\ SiO_2$ catalyst and that after stability testing were studied by XPS. The spectra of Ce 3d, Cu 2p, O 1s and Si 2p electrons for the catalyst were corrected by the C 1s peak

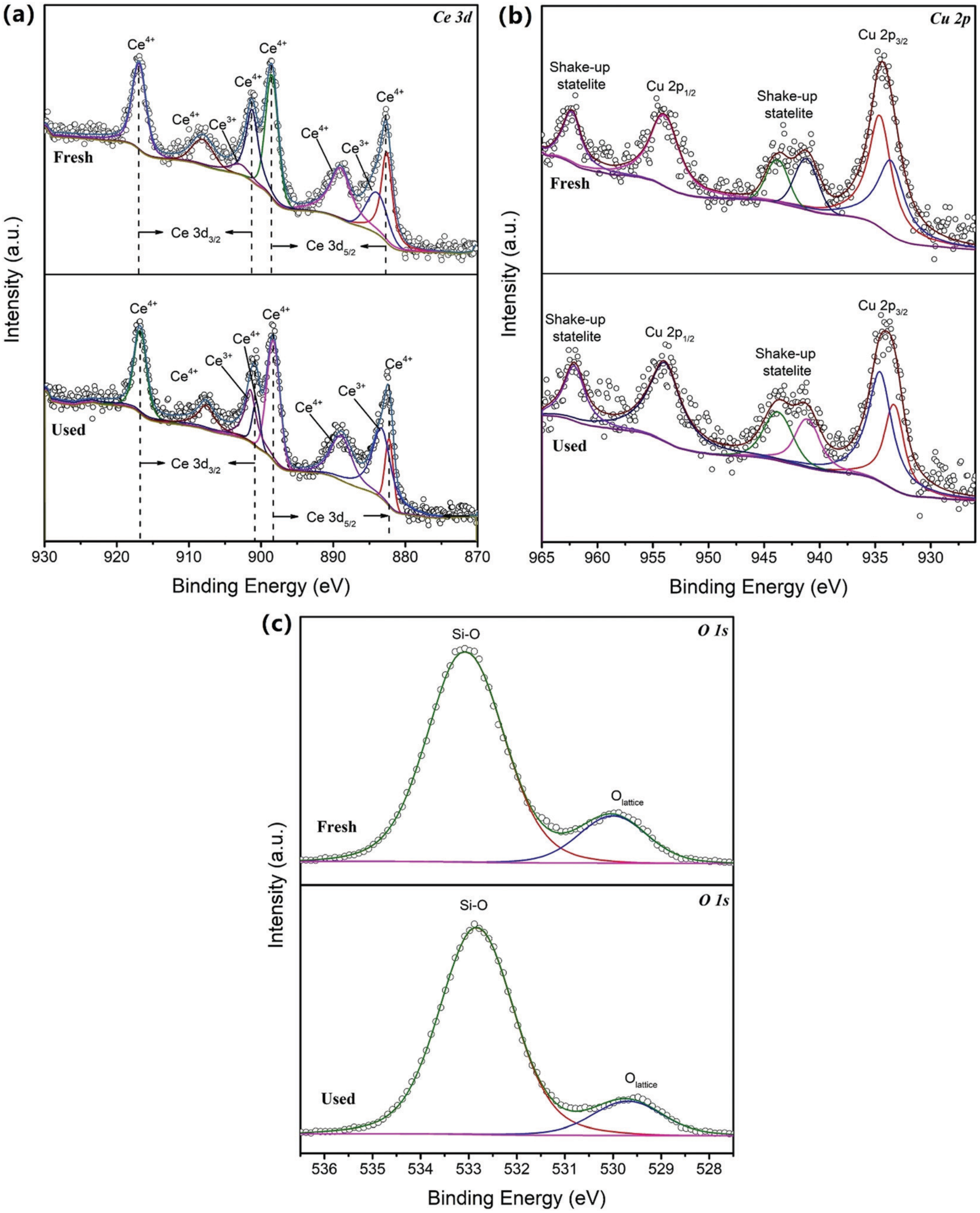

Fig. 8 (a) XPS spectra of Ce 3d, (b) Cu 2p and (c) O 1s in fresh and used $0.5CeO_2/0.25CuO/3DOM\ SiO_2$ catalysts.

at 284.8 eV. The XPS structure of Ce 3d consisted of four pairs of $3d_{5/3}$ and $3d_{3/2}$ peaks, and Ce^{3+} and Ce^{4+} coexisted in the $0.5CeO_2/0.25CuO/3DOM\ SiO_2$ catalyst according to the Ce 3d spectrum shown in Fig. 8a.[41] Except for the peaks at 884.1 eV and 903.1 eV, which belong to the Ce^{3+} state, the other six peaks all come from the Ce^{4+} state.[24,34] Ce^{3+} is most likely formed by oxygen vacancies in the catalyst. Besides, it may be caused by insufficient coordination of Ce^{3+} on the surface of the nano-sized Ce_2O_3 crystals, or the doping of Cu^{2+}.[24,42,43] There is an obvious difference between the used and the fresh sample. The peak of Ce^{3+} is obviously enhanced in the former, which can be considered as the result of oxygen vacancies generated during the reaction. As shown in Fig. 8b, there are two asymmetric broad peaks in the Cu 2p XPS spectrum, Cu $2p_{1/2}$ (929–938 eV) and Cu $2p_{3/2}$ (948–959 eV), which can fit two Cu $2p_{3/2}$ peaks centered at 933.2 eV and 934.7 eV, respectively. The main peak at 934.7 eV is a typical Cu^{2+} state,[44] and the presence of the other two satellite peaks at 942.6 eV and 962.5 eV also indicates that it is a typical feature of Cu^{2+}.[45] It should be noted that it is difficult to accurately distinguish the oxidation state of copper by the location of XPS spectra due to the close binding energy of Cu^+ and Cu^{2+} states.[22,46] Therefore, copper in $0.5CeO_2/0.25CuO/3DOM\ SiO_2$ may have both ions.

The information about the factors influencing catalytic performance can also be obtained from the O 1s XPS spectrum of the fresh and used catalysts, where two O 1s peaks can be fitted to the obtained spectra. The peak near the binding energy of 529.8 eV could be assigned to the lattice oxygen,[24] while the peak near 532.8 eV is the Si–O–Si bond on the 3DOM SiO_2 support.[47] Obviously, lattice oxygen of the used catalyst is significantly consumed compared to the fresh catalyst, indicating that a large number of oxygen vacancies will be generated during the reaction, and these vacancies are supplemented by the migration of bulk lattice oxygen of the metal oxide.[48] This is crucial for the adsorption/dissociation of oxygen in CO oxidation reactions and should play a key role in understanding the reaction mechanism.

3.4 Catalytic performance evaluation

The catalytic activity of the $CeO_2/CuO/3DOM\ SiO_2$ series catalyst was investigated using CO oxidation reaction as a model. To simulate the exhaust gas of a lean fuel engine and obtain the best catalytic performance, an excessive amount of O_2 ($CO/O_2 = 1/10$) was used in the reaction. Meanwhile, to match the standard exhaust conditions of the vehicle, the GHSV was maintained at 120 000 mL g^{-1} h^{-1}.

From Fig. 9a, $1CeO_2/3DOM\ SiO_2$ and $1CuO/3DOM\ SiO_2$ have almost no activity to catalyze CO oxidation below 240 °C compared with other catalysts, indicating the poor activity when using a simple CeO_2 or CuO mono-metal oxide

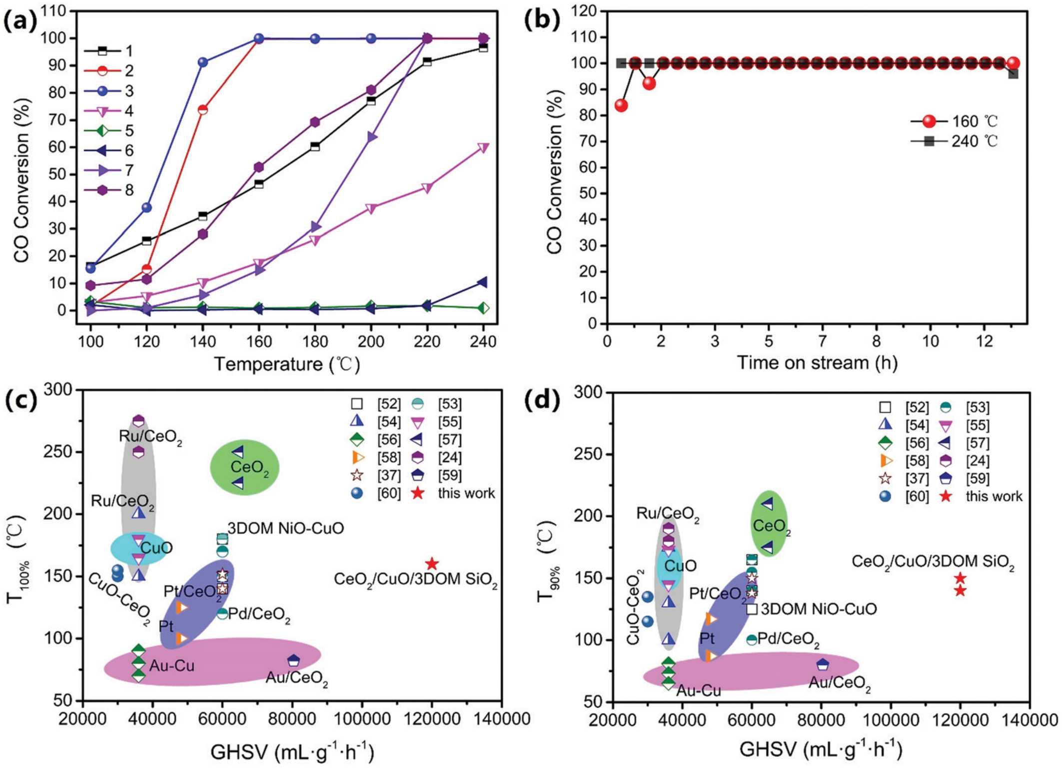

Fig. 9 (a) CO conversion rate as a function of the reaction temperature for various $CeO_2/CuO/3DOM\ SiO_2$ series catalysts. (b) Long-term stability test results of $0.5CeO_2/0.25CuO/3DOM\ SiO_2$ at 160 °C and 240 °C. ((1) $0.75CeO_2/0.5CuO/3DOM\ SiO_2$, (2) $0.5CeO_2/0.5CuO/3DOM\ SiO_2$, (3) $0.5CeO_2/0.25CuO/3DOM\ SiO_2$, (4) $0.25CeO_2/0.25CuO/3DOM\ SiO_2$, (5) $1CeO_2/3DOM\ SiO_2$, (6) $1CuO/3DOM\ SiO_2$, (7) $0.25CeO_2/0.5CuO/3DOM\ SiO_2$, (8) $0.75CeO_2/0.25CuO/3DOM\ SiO_2$). The comparison of CO catalytic oxidation performance of different nanostructured materials (c) $T_{100\%}$ and (d) $T_{90\%}$.[3,19,24,51–57] component as a catalyst, and it is difficult to achieve efficient oxidation of CO at low temperatures. However, the catalytic activity significantly improved after loading both CeO_2 and CuO, indicating that there is strong chemical synergy between CeO_2 and CuO, which is conducive to the CO catalytic oxidation reaction. To study the effect of different loading ratios of CeO_2 and CuO on the catalytic performance, the products with different loading ratios of CeO_2 (0.25, 0.5, and 0.75) were prepared while maintaining the same loading ratios of CuO (0.25 or 0.5), and their catalytic properties were tested.

The results indicate that 100% complete catalytic oxidation of CO could be achieved at 160 °C on $0.5CeO_2/0.25CuO/3DOM$ SiO_2 and $0.5CeO_2/0.5CuO/3DOM$ SiO_2. Meanwhile, the former is better as its activity is significantly higher than that of the latter when the temperature is below 160 °C. The catalytic activity of $CeO_2/CuO/3DOM$ SiO_2 series products is not specifically linearly associated with the CeO_2/CuO ratios, and an appropriate CeO_2/CuO ratio can stimulate their catalytic activity. In addition, the appropriate proportion of CuO will have a favorable effect on the interaction between CeO_2 and CuO. At a low CuO ratio range, Cu^+ (Cu^+ is the active site for CO adsorption) produced by the CeO_2–CuO interaction showed a gradual increment when the CuO content increased, thus promoted the catalytic activity. However, when the proportion of CuO reaches

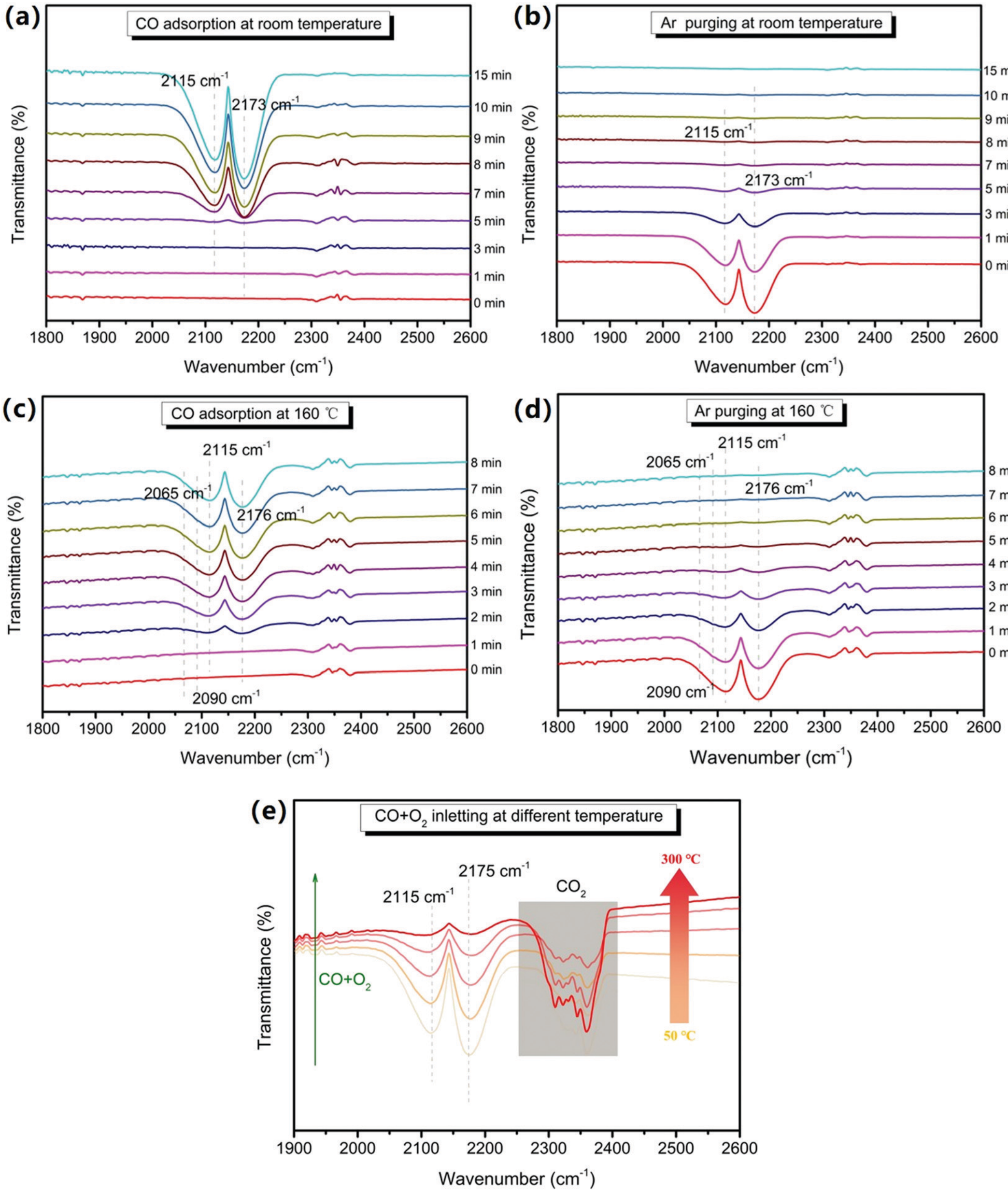

Fig. 10 *In situ* FTIR spectra of CO catalytic oxidation on $0.5CeO_2/0.25CuO/3DOM$ SiO_2 under conditions: (a) CO adsorption at room temperature, (b) Ar purging at room temperature, (c) CO adsorption at 160 °C, (d) Ar purging at 160 °C, and (e) CO_2 evolution in the temperature range of 50–300 °C. (catalyst mass/KBr mass: 1 mg/100 mg; gas flow: 2% CO/N_2, Ar, 20% O_2/N_2, 20 mL min^{-1}).

a critical value, the CuO nanoparticles will agglomerate to generate larger particles, which will cover part of the surface adsorption active sites, leading to a sharp decrease in the Cu^+ content and a weakened interaction between Ce and Cu oxides, resulting in a decreased activity of the catalyst.[49,50]

The CO catalytic oxidation stability of the $0.5CeO_2/0.25CuO/3DOM\ SiO_2$ catalyst at 160 °C and 240 °C for 13 hours was studied (Fig. 9b). The results indicate that the catalyst maintains excellent stability at both temperatures and the CO conversion rate always remains at about 100%. At 160 °C, the unstable conversion rate of the catalyst at the initial stage could be attributed to the insufficient activation of the catalyst. In addition, the performances of $CeO_2/CuO/3DOM\ SiO_2$ and other nanostructured materials were compared (as shown in Fig. 9c and d). $T_{100\%}$ and $T_{90\%}$ (the temperature at which CO achieves 100% and 90% conversion) are two important indexes of the catalytic activity of CO. The two catalysts with better performance prepared in this work can achieve complete conversion at 160 °C, which almost surpasses that of most of the non-precious metal catalysts, whereas the $T_{90\%}$ index of the two catalysts is still slightly inferior to some non-noble metal catalysts. The advantage of $CeO_2/CuO/3DOM\ SiO_2$ over other materials lies in that, and it can achieve 100% conversion of CO under a very large GHSV but at a relatively low temperature range.

3.5 *In situ* FTIR analysis

To determine the adsorption sites and the oxidation process of CO during the oxidation process on the $0.5CeO_2/0.25CuO/3DOM\ SiO_2$ catalyst, *in situ* FTIR technology was selected to monitor the possible real-time radicals at different reaction temperatures. When comparing the CO adsorption at room temperature and 160 °C (Fig. 10a and c), the peak emerged in the range 2000–2250 cm^{-1} belonging to the $Cu^{\delta+}$–CO species.[58] In detail, the infrared vibration band at ~2115 cm^{-1} corresponds to linear CO on Cu^+, and the signal at ~2173 cm^{-1} could be attributed to gas-phase CO.[59] Compared with the IR spectra of CO adsorption at room temperature, weaker infrared signals at 2065 cm^{-1} and 2090 cm^{-1} can be observed during CO adsorption at 160 °C, which could be attributed to the $Cu^{\delta+}$-multicarbonyl species formed by the binding of two or three CO ligands to a $Cu^{\delta+}$ site (Fig. 10c and d).[60,61] Besides, an obvious difference is the longer time for a CO adsorption–desorption recycle on the $0.5CeO_2/0.25CuO/3DOM\ SiO_2$ catalyst at room temperature, and a time period of more than 10 minutes was required for the complete adsorption saturation/desorption process. When the reaction was conducted at 160 °C, the adsorption saturation/desorption is completed in only about 5 minutes. This indicates that the increased temperature can promote the reaction ability to CO on the catalyst surface. The *in situ* IR spectra of the CO oxidation process from 50 to 300 °C are shown in Fig. 10e, and the intensity of the CO-related peaks shows a continuous downward trend. The gaseous CO_2 related band appears at 2300–2400 cm^{-1} with a decrease in the intensity of the CO correlation peaks.[61] The gaseous CO_2 peaks start to appear at 50 °C. In addition, they were enhanced significantly when the temperature increases, which is consistent with the increased CO conversion rate. The appearance of CO_2 peaks at near–room temperature also confirms that the $0.5CeO_2/0.25CuO/3DOM\ SiO_2$ catalyst has an excellent CO oxidation activity under near-RT conditions.

Combining the results of *in situ* FTIR and other characterizations, Fig. 11 concludes the possible mechanisms of CO oxidation over $CeO_2/CuO/3DOM\ SiO_2$. Doping a small amount of Cu^{2+} in the CeO_2 crystal will increase its lattice defects while forming oxygen vacancies and releasing electrons,[59] and the oxygen exchange between adsorbed oxygen and lattice oxygen can enhance this process.[19] The O_2 molecules and CO molecules first diffuse rapidly in the macropores of 3DOM SiO_2. The synergistic effect of copper and cerium follows the avenue:

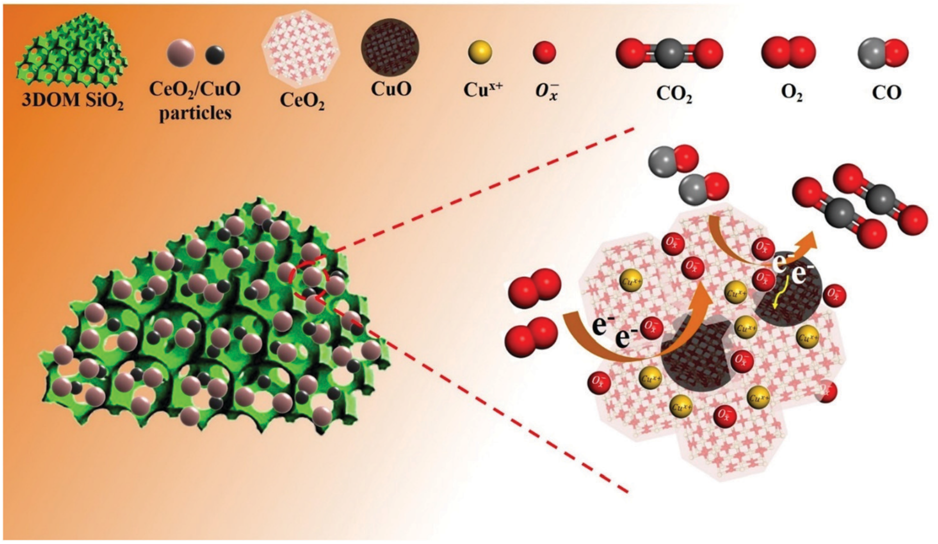

Fig. 11 Proposed possible mechanisms for CO oxidation over the $CeO_2/CuO/3DOM\ SiO_2$ catalyst.

$Cu^{2+} + Ce^{3+} \rightarrow Cu^{+} + Ce^{4+}$, which often occurs at the doped site and will lead to an increase in the active oxygen content of the catalyst. CO is adsorbed on Cu-doped CeO_2 active sites on the surface and will react with the adjacent oxygen anion O_x^- to generate CO_2. Then, the CO_2 desorption process will create oxygen vacancies, which will be refilled rapidly by O_2 molecules from the feed flow and is ready to react in the next step.[61,62] The possible reaction processes are as follows:

$$O \rightarrow \frac{1}{2}O_2 + V_O^{\bullet\bullet} + 2e^- \quad (2)$$

$$O_{2gas} \rightarrow O_{2ads} \quad (3)$$

$$O_{2ads} + ne^- \rightarrow O_{x,ads}^- \quad (4)$$

$$CO_{gas} \rightarrow CO_{ads} \quad (5)$$

$$CO_{ads} + O_{x,ads}^- \rightarrow CO_2 + e^- \quad (6)$$

4. Conclusions

$CeO_2/CuO/3DOM\ SiO_2$ composite catalysts were prepared by a colloidal crystal template method and a simple grinding calcination method. The products showed much high conversion efficiency toward CO due to the high mass transport efficiency of the 3DOM structure and synergistic effects in the composite catalysis. Among all of the as-prepared samples, $0.5CeO_2/0.25CuO/3DOM\ SiO_2$ showed the highest catalytic activity for CO oxidation, which achieved complete CO conversion at 160 °C and showed excellent stability. *In situ* FTIR spectroscopy indicated that Cu^+ was the main adsorption site for CO. Combining the results of *in situ* FTIR and other characterizations, the possible mechanism for the CO oxidation on $CeO_2/CuO/3DOM\ SiO_2$ was supposed to be the reaction between adsorbed CO on the Cu^+ active sites and the adjacent oxygen anions O_x^- to form CO_2, which rapidly diffuse and separate in the 3DOM SiO_2 channel, thereby realizing the efficient conversion of CO. This work manifests that the $CeO_2/CuO/3DOM\ SiO_2$ composite has potential applications in reducing CO exhaust pollution and overcoming other environmental problems caused by CO.

Conflicts of interest

There are no conflicts to declare.

Acknowledgements

This work was supported by the National Natural Science Fund of China (5774331), the ShengHua Scholar Project of CSU (20160201).

References

1 K. S. Abdel Halim, A. M. Ismail, M. H. Khedr and M. F. Abadir, Catalytic oxidation of CO gas over nanocrystallite $Cu_xMn_{1-x}Fe_2O_4$, *Top. Catal.*, 2008, **47**, 66–72.

2 Z. L. Yan, H. M. Yang, J. Ouyang and A. D. Tang, *In situ* loading of highly-dispersed CuO nanoparticles on hydroxylgroup-rich SiO_2–AlOOH composite nanosheets for CO catalytic oxidation, *Chem. Eng. J.*, 2017, **316**, 1035–1046.

3 X. Yang, X. Cheng, J. Ma, Y. Zou, W. Luo and Y. Deng, Large-pore mesoporous CeO_2–ZrO_2 solid solutions with in-pore confined Pt nanoparticles for enhanced CO oxidation, *Small*, 2019, **15**, e1903058.

4 M. T. Zhu, K. F. Zhang, W. P. Du, A. P. Jia, M. F. Luo and J. Q. Lu, Highly active and water tolerant Pt/MFe_2O_4 (M = Co and Ni) catalysts for low temperature CO oxidation, *Appl. Catal., A*, 2021, **619**, 118142.

5 C. He, J. Cheng, X. Zhang, M. Douthwaite and Z. Hao, Recent advances in the catalytic oxidation of volatile organic compounds: A review based on pollutant sorts and sources, *Chem. Rev.*, 2019, **119**, 7.

6 C. Yang, G. Miao, Y. Pi, Q. Xia, J. Wu, Z. Li and J. Xiao, Abatement of various types of VOCs by adsorption/catalytic oxidation: A review, *Chem. Eng. J.*, 2019, **370**, 1128–1153.

7 M. S. Kamal, S. A. Razzak and M. M. Hossain, Catalytic oxidation of volatile organic compounds (VOCs) – A review, *Atmos. Environ.*, 2016, **140**, 117–134.

8 A. I. Boronin, E. M. Slavinskaya, A. Figueroba, A. I. Stadnichenko, T. Y. Kardash, O. A. Stonkus, E. A. Fedorova, V. V. Muravev, V. A. Svetlichnyi, A. Bruix and K. M. Neyman, CO oxidation activity of Pt/CeO_2 catalysts below 0 °C: Platinum loading effects, *Appl. Catal., B*, 2021, **286**, 119931.

9 B. Qiao, A. Wang, X. Yang, L. F. Allard, Z. Jiang, Y. Cui, J. Liu, J. Li and T. Zhang, Single-atom catalysis of CO oxidation using Pt_1/FeO_x, *Nat. Chem.*, 2011, **3**, 634–641.

10 B. J. Cha, S. Y. Kim, C. M. Choi, J. Y. Sung, M. C. Choi, H. O. Seo and Y. D. Kim, Ultra-low loading of iron oxide on Pt/Al_2O_3 for enhanced catalytic activity of CO oxidation at room temperature: A simple method for applications, *Chem. Eng. J.*, 2021, **404**, 126560.

11 F. Bi, X. Zhang, Q. Du, K. Yue and Y. Huang, Influence of pretreatment conditions on low-temperature CO oxidation over Pd supported UiO-66 catalysts, *Mol. Catal.*, 2021, **509**, 111633.

12 T. G. Mi, Y. W. Wu, M. X. Xu, X. Y. Zhou and Q. Lu, Theoretical insights into the roles of active oxygen species in heterogeneous oxidation of CO over Mn/TiO_2 catalyst, *Appl. Catal., A*, 2021, **616**, 118104.

13 X. Wang, J. A. Rodriguez, J. C. Hanson, D. Gamarra, A. Martinez-Arias and M. Fernandez-Garcia, Unusual physical and chemical properties of Cu in $Ce_{(1-x)}Cu_{(x)}O_{(2)}$ oxides, *Cheminform*, 2010, **109**, 19595–19603.

14 T. S. Cam, S. O. Omarov, M. I. Chebanenko, A. S. Sklyarova and V. I. Popkov, One step closer to the low-temperature CO oxidation over non-noble CuO/CeO_2 nanocatalyst: the effect of CuO loading, *J. Environ. Chem. Eng.*, 2021, **9**, 105373.

15 Y. Tang, Y. Wei, Z. Wang, S. Zhang, Y. Li, L. Nguyen, Y. Li, Y. Zhou, W. Shen, F. F. Tao and P. Hu, Synergy of single-atom Ni_1 and Ru_1 sites on CeO_2 for dry reforming of CH_4, *J. Am. Chem. Soc.*, 2019, **141**, 7283–7293.

16 A. M. Lacoste, I. S. Tiscornia, M. Bonne, L. Michelin and A. V. Boix, Study of CuO–CeO_2 catalysts supported on

ordered porous silica with different mesostructure and morphology. Influence on CO preferential oxidation, *Microporous Mesoporous Mater.*, 2021, **320**, 111094.

17 C. Loschen, A. Migani, S. T. Bromley, F. Illas and K. M. Neyman, ChemInform abstract: Density functional studies of model cerium oxide nanoparticles, *ChemInform*, 2008, **39**, 5730–5738.

18 S. Y. Zhang, H. Liu, C. C. Sun, P. Liu, L. Li, Z. Yang, X. Feng, F. Huo and X. Lu, CuO/Cu_2O porous composites: Shape and composition controllable fabrication inherited from metal organic frameworks and further application in CO oxidation, *J. Mater. Chem. A*, 2015, **3**, 5294–5298.

19 X. Zhang, W. Z. Li, Z. Zhou, K. Chen, M. W. Wu and L. Yuan, High dispersed Pd supported on CeO_2(100) for CO oxidation at low temperature, *Mol. Catal.*, 2021, **508**, 111580.

20 A. Martínez-Arias, D. Gamarra, A. Hungría, M. Fernández-García, G. Munuera, A. Hornés, P. Bera, J. Conesa and A. Cámara, Characterization of active sites/entities and redox/catalytic correlations in copper-ceria-based catalysts for preferential oxidation of CO in H_2-rich streams, *Catalysts*, 2013, **3**, 378–400.

21 A. Cámara, V. Corberán and A. Martínez-Arias, Inverse CeO_2/CuO WGS catalysts: Influence of the presence of oxygen in the reactant mixture, *Catal. Today*, 2021, **363**, 105–110.

22 M. Lykaki, E. Pachatouridou, S. A. C. Carabineiro, E. Iliopoulou, C. Andriopoulou, N. Kallithrakas-Kontos, S. Boghosian and M. Konsolakis, Ceria nanoparticles shape effects on the structural defects and surface chemistry: Implications in CO oxidation by Cu/CeO_2 catalysts, *Appl. Catal., B*, 2018, **230**, 18–28.

23 P. A. DeSario, C. L. Pitman, D. J. Delia, D. M. Driscoll, A. J. Maynes, J. R. Morris, A. M. Pennington, T. H. Brintlinger, D. R. Rolison and J. J. Pietron, Low-temperature CO oxidation at persistent low-valent Cu nanoparticles on TiO2 aerogels, *Appl. Catal., B*, 2019, **252**, 205–213.

24 J. Li, Z. Liu, D. A. Cullen, W. Hu, J. Huang, L. Yao, Z. Peng, P. Liao and R. Wang, Distribution and valence state of Ru species on CeO_2 supports: Support shape effect and its influence on CO oxidation, *ACS Catal.*, 2019, **9**, 11088–11103.

25 I. Y. Kaplin, E. S. Lokteva, E. V. Golubina, V. Shishova, K. I. Maslakov, A. V. Fionov, O. Y. Isaikina and V. Lunin, Efficiency of manganese modified CTAB-templated ceria-zirconia catalysts in total CO oxidation, *Appl. Surf. Sci.*, 2019, **485**, 432–440.

26 Y. Jiang, L. Shi, Y. Huang, J. Gao, X. Zhang and L. Zhou, Preparation of robust biocatalyst based on cross-linked enzyme aggregates entrapped in three-dimensionally ordered macroporous silica, *ACS Appl. Mater. Interfaces*, 2014, **6**, 2622–2628.

27 D. Fattakhova-Rohlfing, A. Zaleska and T. Bein, Three-dimensional titanium dioxide nanomaterials, *Chem. Rev.*, 2014, **114**, 9487–9558.

28 M. Wang, X. Wang, Q. Yue, Y. Zhang, C. Wang, J. Chen, H. Cai, H. Lu, A. A. Elzatahry, D. Zhao and Y. Deng, Templated fabrication of core–shell magnetic mesoporous carbon microspheres in 3-dimensional ordered macroporous silicas, *Chem. Mater.*, 2014, **26**, 3316–3321.

29 P. Tian, K. Shen, J. Chen, T. Fan, R. Fang and Y. Li, Self-templated formation of Pt@ZIF-8/SiO_2 composite with 3D-ordered macropores and size-selective catalytic properties, *Small*, 2018, **2**, 1800219.

30 B. Jmsa, B. Ptw, S. Ye, D. Dy, D. Hy and Z. E. Hui, Comparison of waste plastics pyrolysis under nitrogen and carbon dioxide atmospheres: A thermogravimetric and kinetic study, *J. Anal. Appl. Pyrol.*, 2021, **156**, 105135.

31 A. S. Patole, S. P. Patole, S. Y. Jung, J. B. Yoo, J. H. An and T. H. Kim, Self assembled graphene/carbon nanotube/polystyrene hybrid nanocomposite by in situ microemulsion polymerization, *Eur. Polym. J.*, 2012, **48**, 252–259.

32 F. Farivar, L. Y. Pei, K. Hassan, T. T. Tung, D. Losic, A. J. Pollard and D. Losic, Unlocking thermogravimetric analysis (TGA) in the fight against ''fake graphene'' materials, *Carbon*, 2021, **179**, 505–513.

33 Y. Deng, X. Shi, L. Wei, H. Liu and B. Li, Effect of intergrowth and coexistence CuO–CeO_2 catalyst by grinding method application in the catalytic reduction of NO_x by CO, *J. Alloys Compd.*, 2021, **869**, 159231.

34 Y. Xie, J. F. Wu, G. J. Jing, H. Zhang, S. H. Zeng, X. P. Tian, X. Y. Zou, W. Jing, S. H. Quan and Z. C. Jian, Structural origin of high catalytic activity for preferential CO oxidation over CuO/CeO_2 nanocatalysts with different shapes, *Appl. Catal., B*, 2018, **239**, 665–676.

35 P. Djinović, J. Batista and A. Pintar, Calcination temperature and CuO loading dependence on CuO–CeO_2 catalyst activity for water–gas shift reaction, *Appl. Catal., A*, 2008, **347**, 23–33.

36 S. T. Hossain, E. Azeeva, K. F. Zhang, E. T. Zell, D. T. Bernard, S. Balaz and R. G. Wang, A comparative study of CO oxidation over Cu–O–Ce solid solutions and CuO/CeO_2 nanorods catalysts, *Appl. Surf. Sci.*, 2018, **455**, 132–143.

37 J. Rouquerol, F. Rouquerol and K. Sing, *Adsorption by Powders and Porous Solids, Principles, Methodology and Applications*, 1999.

38 J. C. Groen, L. A. A. Peffer and J. Pérez-Ramírez, Pore size determination in modified micro- and mesoporous materials. Pitfalls and limitations in gas adsorption data analysis, *Microporous Mesoporous Mater.*, 2003, **60**, 1–17.

39 U. Kuila and M. Prasad, Specific surface area and pore-size distribution in clays and shales, *Geophys. Prospect*, 2013, **62**, 196.

40 G. Ji, M. Li, G. Li, G. Gao, H. Zou, S. Gan and X. Xu, Hydrothermal synthesis of hierarchical micron flower-like γ-AlOOH and γ-Al_2O_3 superstructures from oil shale ash, *Powder Technol.*, 2012, **215**, 54–58.

41 J. Zheng, Z. Chen, J. Fang, Z. Wang and S. Zuo, MCM-41 supported nano-sized CuO–CeO_2 for catalytic combustion of chlorobenzene, *J. Rare Earths*, 2020, **38**, 933–940.

42 I. S. Tiscornia, A. M. Lacoste, L. Gómez and A. V. Boix, CuO–CeO_2/SiO_2 coating on ceramic monolith: Effect of the nature

of the catalyst support on CO preferential oxidation in a H_2-rich stream, *Int. J. Hydrogen Energy*, 2020, **45**, 6636–6650.

43 E. Paparazzo, G. M. Ingo and N. Zacchetti, X-ray induced reduction effects at CeO_2 surfaces: An X-ray photoelectron spectroscopy study, *J. Vac. Sci. Technol., A*, 1991, **9**, 1416–1420.

44 L. Wang, B. Zhu, S. Zhang and W. Huang, Flower-like Au–CuO/Bi_2WO_6 microsphere catalysts: Synthesis, characterization, and their catalytic performances for CO oxidation, *Catalysts*, 2017, **7**, 266.

45 J. L. Cao, Y. Wang, X. L. Yu, S. R. Wang, S. H. Wu and Z. Y. Yuan, Mesoporous CuO–Fe_2O_3 composite catalysts for low-temperature carbon monoxide oxidation, *Appl. Catal., B*, 2008, **79**, 26–34.

46 S. Gong, A. Wang, J. Zhang, J. Guan, N. Han and Y. Chen, Gram-scale synthesis of ultra-fine Cu_2O for highly efficient ozone decomposition, *RSC Adv.*, 2020, **10**, 5212–5219.

47 Z. L. Yan, L. J. Fu, X. C. Zuo and H. M. Yang, Green assembly of stable and uniform silver nanoparticles on 2D silica nanosheets for catalytic reduction of 4-nitrophenol, *Appl. Catal., B*, 2018, **226**, 23–30.

48 L. Zhang, T. Chen, S. Zeng and H. Su, Effect of doping elements on oxygen vacancies and lattice oxygen in CeO_2–CuO catalysts, *J. Environ. Chem. Eng.*, 2016, **4**, 2785–2794.

49 X. Guo, Z. Qiu, J. Mao and R. Zhou, Shape-controlled $Cu_xCe_{1-x}O_2$ nanorods catalyst and the active components functioned in selective oxidation of CO in hydrogen-rich stream, *J. Power Sources*, 2020, **451**, 227757.

50 P. Zhu, L. Jing, S. Zuo and R. Zhou, Preferential oxidation properties of CO in excess hydrogen over CuO–CeO_2 catalyst prepared by hydrothermal method, *Appl. Surf. Sci.*, 2008, **255**, 2903–2909.

51 A. Rastegarpanah, Y. X. Liu, J. G. Deng, L. Jing, W. B. Pei, X. Zhang, Z.q. Hou, M. Rezaei and H. X. Dai, Influence of preparation method on catalytic performance of three-dimensionally ordered macroporous NiO–CuO for CO oxidation, *J. Solid State Chem.*, 2021, **297**, 122091.

52 R. Rangel, E. González-A, A. Solís-García, T. A. Zepeda, D. H. Galván, A. Gómez-Cortés and G. Díaz, Pt and Ir supported on mixed $Ce_{0.97}Ru_{0.03}O_2$ oxide as low-temperature CO oxidation catalysts, *Catal. Today*, 2021, DOI: 10.1016/j.cattod.2021.03.017.

53 W. Liu, B. Q. Wang, C. C. Cui, Y. W. Zhang, L. X. Wang and Z. P. Wang, The surface restructuring of copper oxides with mixed oxidation-states and their efficient CO oxidation properties, *Mater. Lett.*, 2021, **289**, 129378.

54 S. Dey and N. S. Mehta, Influence the performances of hopcalite catalysts by the addition of gold nanoparticle for low temperature CO oxidation, *Cleaner Eng. Tech.*, 2021, **4**, 100171.

55 Y. Wang, D. Li, K. Li and R. Farrauto, Enhanced propane and carbon monoxide oxidation activity by structural interactions of CeO_2 with MnO_x/Nb_2O_{5-x} catalysts, *Appl. Catal., B*, 2020, **267**, 118363.

56 J. Ding, L. Li, Y. Wang, H. Li, M. Yang and G. Li, Topological transformation of LDH nanosheets to highly dispersed PtNiFe nanoalloys enhancing CO oxidation performance, *Nanoscale*, 2020, **12**, 14882–14894.

57 L. L. Zhou, S. Wei, W. W. Wang, Z. Jin and C. J. Jia, Au/La-CeO catalyst for CO oxidation: Effect of different atmospheres pretreatment on gold state – commemorating the 100th anniversary of the birth of Academician Guangxian Xu, *J. Rare Earths*, 2021, **39**, 364–373.

58 Z. Guo, L. Song, T. Xu, D. Gao, C. Li, X. Hu and G. Chen, CeO_2–CuO bimetal oxides derived from Ce-based MOF and their difference in catalytic activities for CO oxidation, *Mater. Chem. Phys.*, 2019, **226**, 338–343.

59 W. W. Wang, W. Z. Yu, P. P. Du, H. Xu, Z. Jin, R. Si, C. Ma, S. Shi, C. J. Jia and C. H. Yan, Crystal plane effect of ceria on supported copper oxide cluster catalyst for CO oxidation: Importance of metal–support interaction, *ACS Catal.*, 2017, **7**, 1313–1329.

60 Z. Jiang, Y. Yang, W. Shangguan and Z. Jiang, Influence of support and metal precursor on the state and CO catalytic oxidation activity of platinum supported on TiO_2, *J. Phys. Chem. C*, 2012, **116**, 19396–19404.

61 Y. Fang, X. Chi, L. Li, J. Yang, S. Liu, X. Lu, W. Xiao, L. Wang, Z. Luo, W. Yang, S. Hu, J. Xiong, S. Hoang, H. Deng, F. Liu, L. Zhang, P. Gao, J. Ding and Y. Guo, Elucidating the nature of the Cu(I) active site in CuO/TiO_2 for excellent low-temperature CO oxidation, *ACS Appl. Mater. Interfaces*, 2020, **12**, 7091–7101.

62 K. Kim, J. D. Yoo, S. Lee, M. Bae, J. Bae, W. Jung and J. W. Han, A simple descriptor to rapidly screen CO oxidation activity on rare-earth metal-doped CeO_2: From experiment to first-principles, *ACS Appl. Mater. Interfaces*, 2017, **9**, 15449–15458.